J. Fluid Mech. (2009), *vol.* 618, *pp.* 89–112.
doi:10.1017/S0022112008003947 Printed in the United Kingdom

Analysis of the thermal plumes in turbulent Rayleigh–Bénard convection based on well-resolved numerical simulations

M. KACZOROWSKI† AND C. WAGNER

DLR – Institute of Aerodynamics and Flow Technology, Bunsenstr. 10, 37073 Göttingen, Germany

(Received 7 February 2008 and in revised form 29 August 2008)

In this study, direct numerical simulations and high-resolved large eddy simulations of turbulent Rayleigh–Bénard convection were conducted with a fluid of Prandtl number $Pr = 0.7$ in a long rectangular cell of aspect ratio unity in the cross-section and periodic boundaries in a horizontal longitudinal direction. The analysis of the thermal and kinetic energy spectra suggests that temperature and velocity fields are correlated within the thermal boundary layers and tend to be uncorrelated in the core region of the flow. A tendency of decorrelation of the temperature and velocity fields is also observed for increasing Ra when the flow has become fully turbulent, which is thought to characterize this regime. This argument is also supported by the analysis of the correlation of the turbulent fluctuations $|\boldsymbol{u}|'$ and θ'. The plume and mixing layer dominated region is found to be separated from the thermal dissipation rates of the bulk and conductive sublayer by the inflection points of the probability density function (PDF). In order to analyse the contributions of bulk, boundary layers and plumes to the mean heat transfer, the thermal dissipation rate PDFs of four different Ra are integrated over these three regions. Hence, it is shown that the core region is dominated by the turbulent fluctuations of the thermal dissipation rate throughout the range of simulated Ra, whereas the contributions from the conductive sublayer due to turbulent fluctuations increase rapidly with Ra. The latter contradicts results by He, Tong & Xia (*Phys. Rev. Lett.*, vol. 98, 2007). The results also show that the plumes and mixing layers are increasingly dominated by the mean gradient contributions. The PDFs of the core region are compared to an analytical scaling law for passive scalar turbulence which is found to be in good agreement with the results of the present study. It is noted that the core region scaling seems to approach the behaviour of a passive scalar as Ra increases, i.e. it changes from pure exponential to a stretched exponential scaling.

1. Introduction

Rayleigh–Bénard convection is one of the classical problems in fluid mechanics where a fluid of Prandtl number $Pr = \hat{\nu}/\hat{\kappa}$ is typically bound by a bottom and a top wall which are heated and cooled, respectively. The Rayleigh number

$$Ra = \hat{\alpha}\hat{g}\hat{H}^3\frac{\Delta\hat{T}}{\hat{\nu}\hat{\kappa}} \tag{1.1}$$

† Email address for correspondence: matthias.kaczorowski@dlr.de

is a non-dimensional parameter for the measure of the ratio of buoyancy and diffusive forces, where $\hat{\alpha}$, $\hat{\nu}$ and $\hat{\kappa}$ denote the thermal expansion coefficient, the kinematic viscosity and the thermal diffusivity, respectively, $\hat{g}$ is the gravitational acceleration, $\hat{H}$ the height of the fluid layer and $\Delta\hat{T}$ the vertical temperature difference (we denote dimensional quantities with $\hat{}$ and dimensionless without).

For decades there has been discussion of the scaling of the Nusselt–Rayleigh relation, i.e. $Nu \sim Ra^{\beta}$, where the Nusselt number $Nu = |\partial\hat{T}/\partial\hat{z}|_{wall}\hat{H}/\Delta\hat{T}$ is a measure for the effectivity of the convective heat transport and $\hat{z}$ denotes the vertical direction. The scaling and structure of the thermal boundary layers along the axis of a cylindrical container was studied in great detail by du Puits *et al.* (2007) for a wide range of aspect ratios and $10^9 \leqslant Ra \leqslant 10^{12}$. They found that the shape of the boundary layer is almost independent of the cell's aspect ratio. Maystrenko, Resagk & Thess (2007) performed detailed temperature measurements in the thermal boundary layers at different positions in a long rectangular cell and found that the structure of the thermal boundary layer changes significantly in the longitudinal direction which they considered to be an effect of the mean flow properties.

As far as the Nusselt–Rayleigh relation is concerned various experiments in a wide range of Rayleigh numbers found almost as many exponents, e.g. Roche, Castaing & Hebral (2001) obtained $\beta = 0.5$ for $Ra > 10^{12}$. Niemela *et al.* (2000) used Helium near its critical point in order to conduct measurements in a cylindrical container with $10^6 \leqslant Ra \leqslant 10^{17}$. After accounting for the finite conductivity effects of the lateral walls they obtained an exponent $\beta = 0.32$, whereas Castaing *et al.* (1989) measured $\beta \approx 0.286$ in the range $4 \times 10^7 \leqslant Ra \leqslant 10^{12}$. In order to explain the discrepancy of their exponent with other measurements they proposed a new theoretical model accounting for the plumes separating from the boundary layers. In contrast to the classical 1/3-scaling or the 1/2-scaling suggested by Kraichnan (1962) this leads to an exponent of $\beta = 2/7$ which is in good agreement with their measurements and results by Shraiman & Siggia (1990).

Direct numerical simulations (DNS) by Verzicco & Camussi (2003*a*, *b*) in a slender cylindrical cell filled with fluid of $Pr = 0.7$ indicated that with increasing Rayleigh number fluctuations of the velocity field began to dominate within the centre of the cell. This behaviour was not found for the fluctuations of the temperature field, where the thermal dissipation rates in the cell centre were found to vanish for $Ra \to \infty$.

Grossmann & Lohse (2000, 2004) split the thermal dissipation rates $\hat{\epsilon}_\theta = \hat{\kappa}(\partial\hat{T}/\partial\hat{x}_i)^2$ into contributions from plumes (pl) and turbulent background (bg) rather than boundary layers (bl) and bulk, which is used for the kinetic dissipation rates $\hat{\epsilon}_u = \hat{\nu}(\partial\hat{u}/\partial\hat{x}_i)^2$, where $\hat{u}_i$ is the velocity component in direction $\hat{x}_i$ and $\hat{T}$ denotes the temperature:

$$\hat{\epsilon}_u = \hat{\epsilon}_{u,bl} + \hat{\epsilon}_{u,bulk}, \tag{1.2}$$

$$\hat{\epsilon}_\theta = \hat{\epsilon}_{\theta,pl} + \hat{\epsilon}_{\theta,bg}. \tag{1.3}$$

From their subsequent theory they deduced an effective exponent $\beta \approx 0.29$ for the Prandtl number regime $Pr \approx 1, \ldots, 7$, but also pointed out that there is no universal Nu–Ra scaling.

He, Tong & Xia (2007) experimentally measured the thermal dissipation rates of Rayleigh–Bénard convection in a cylindrical cell filled with water. Decomposing the thermal dissipation rates into contributions due to the mean temperature gradient $\hat{\epsilon}_{\bar{\theta}} = \hat{\kappa}(\partial\bar{\hat{T}}/\partial\hat{x}_i)^2$ and the fluctuating components $\bar{\hat{\epsilon}}_{\theta'} = \bar{\hat{\epsilon}}_\theta - \hat{\epsilon}_{\bar{\theta}}$, where $\bar{\hat{\epsilon}}_\theta = \hat{\kappa}\overline{(\partial\hat{T}/\partial\hat{x}_i)^2}$ is the mean thermal dissipation rate, they found that in the bulk region of the cell

contributions due to the mean temperature gradient are negligible, i.e.

$$\bar{\tilde{\epsilon}}_\theta \approxeq \bar{\tilde{\epsilon}}_{\theta'} \tag{1.4}$$

and $\bar{\tilde{\epsilon}}_{\theta'} \sim Ra^{-0.33}$ was obtained for various locations outside the boundary layer. On the other hand, within the boundary layers the fluctuating component amounted to less than 1.5 % of the overall thermal dissipation rate

$$\bar{\tilde{\epsilon}}_\theta \approxeq \hat{\epsilon}_{\bar{\theta}}, \tag{1.5}$$

where a scaling $\hat{\epsilon}_{\bar{\theta}} \sim Ra^{0.63}$ was obtained. He *et al.* (2007) concluded that the above scalings reflect an increasing dissipation of the thermal plumes, leading to a reduction in the temperature fluctuations in the bulk and an increasing mean gradient near the conducting walls, respectively. Therefore, they argued that thermal plumes and boundary layers are two different dynamic structures which cannot be treated equally as suggested by Grossmann & Lohse (2004).

Shishkina & Wagner (2006) also studied the Ra dependence of the thermal dissipation rates by means of DNS, but in contrast to Verzicco & Camussi (2003*a*, *b*) and He *et al.* (2007) they analysed instantaneous flow fields. They showed that the relative contribution from the small scales $\epsilon_\theta \ll \epsilon_{\theta,max}$, where $\epsilon_{\theta,max}$ is the largest thermal dissipation rate found in the volume, continuously increases with Rayleigh number as well as their percentage of the fluid volume. Hence, they concluded that the turbulent background, which is associated with small temperature gradients, dominates the flow field for $Ra \to \infty$. At this point it has to be pointed out that the results by Shishkina & Wagner (2006) are based on a volume-integrated analysis trying to estimate the contributions of different scales to the mean heat transfer, whereas the scalings (1.4) and (1.5) are based on time-averaged quantities that would have to be integrated over the volume they represent. Recently, Shishkina & Wagner (2008) managed to extract sheet-like thermal plumes from the bulk region of an aspect ratio unity Rayleigh cell filled with fluid of $Pr = 5.4$. Hence, it was possible to investigate the properties of the thermal plumes numerically. Aspects of the local heat transfer were analysed by Shishkina & Wagner (2007*b*).

However, the understanding of the heat transfer mechanisms and the regions contributing to the mean heat transfer is still incomplete. In the present study the instantaneous thermal dissipation rates are therefore analysed over a long period of time rather than a single instantaneous flow field. Time series are compared for different Ra from the onset of turbulence until a fully developed turbulent flow is achieved. This allows us to distinguish between the contributions of certain features of the flow, such as boundary layers, plumes and the bulk – and hence quantify their respective contributions to the volume-averaged mean thermal dissipation rate and evaluate their respective behaviour as a function of Ra. Thus, it is possible to obtain a more complete picture of the distribution and behaviour of the thermal dissipation rates and the interaction between the temperature and velocity fields in turbulent Rayleigh–Bénard convection.

In § 2 an overview of the numerical procedure and the resolution of the flow field is provided. Section 3 discusses the differences between the temperature and velocity fields and their changes with Ra. Here, the influence of the wall distance and the Rayleigh number on the turbulent thermal and kinetic energies and the correlation between the temperature and the velocity fields are investigated. The thermal dissipation rates are analysed in § 4 by means of probability density functions, and the contributions of different features of the flow to the mean heat transfer

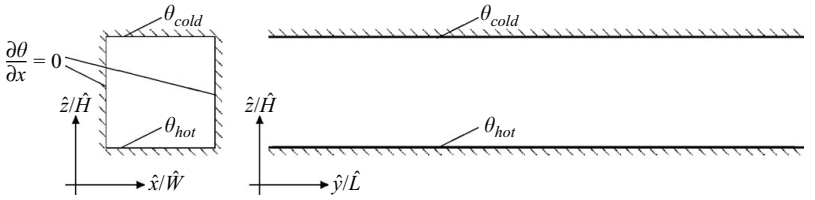

FIGURE 1. Front and side view of the convection cell with temperature boundary conditions.

are estimated and the main heat transfer mechanisms are evaluated. Finally, the conclusions are drawn in § 5.

2. Numerical procedure and resolution requirements

The present numerical simulations are conducted in a cubic geometry of squared cross-section with $\Gamma = \hat{W}/\hat{H} = 1$, where $\hat{H}$ is the height and $\hat{W}$ the width of the enclosed fluid. Periodic boundaries are employed in the longitudinal direction with a length $\hat{L} = 5\hat{H}$ of the fluid (see figure 1). The horizontal walls are assumed to be isothermal with non-dimensional temperatures $\theta_{hot} = +0.5$ and $\theta_{cold} = -0.5$ at the bottom and the top walls, respectively. The adiabatic lateral periodic walls are implemented by means of a zero temperature gradient perpendicular to the wall, i.e. $\partial\theta/\partial x = 0$. No-slip and impermeability conditions are used for the solid walls, so that velocities in i-direction $u_i|_{wall} = 0$.

The non-dimensionalization $x_i = \hat{x}_i/\hat{W}$, $u_i = \hat{u}_i/(\hat{\alpha}\hat{g}\Delta\hat{T}\hat{H})^{1/2}$, $\theta = (\hat{T} - \hat{T}_0)/\Delta\hat{T}$, $p = \hat{p}/(\hat{\rho}\hat{\alpha}\hat{g}\hat{H}\Delta\hat{T})$ and $t = \hat{t}(\hat{\alpha}\hat{g}\Delta\hat{T}\hat{H})^{1/2}/\hat{W}$ is used in order to solve the incompressible Navier–Stokes equations, where density variations are accounted for through the Boussinesq approximation.

$$\left.\begin{aligned} \frac{\partial\langle u_i\rangle}{\partial x_i} &= 0, \\ \frac{\partial\langle u_i\rangle}{\partial t} + \langle u_j\rangle\frac{\partial\langle u_i\rangle}{\partial x_j} + \frac{\partial\tau_{ij}}{\partial x_j} + \frac{\partial\langle p\rangle}{\partial x_i} &= \nu\frac{\partial^2\langle u_i\rangle}{\partial x_j^2} + \langle\theta\rangle\delta_{3i}, \\ \frac{\partial\langle\theta\rangle}{\partial t} + \langle u_i\rangle\frac{\partial\langle\theta\rangle}{\partial x_i} + \frac{\partial h_i}{\partial x_i} &= \kappa\frac{\partial^2\langle\theta\rangle}{\partial x_i^2}. \end{aligned}\right\} \tag{2.1}$$

Here, $u_i (i = x, y, z)$ are the velocity components in i-direction, θ and p represent the temperature and pressure, respectively, and δ_{ij} is the Kronecker symbol; in this case gravitational forces act in z-direction, i.e. the vertical direction. $\langle\cdot\rangle$ denotes volumetric averaging over any finite volume V_i. τ_{ij} and h_i are the subgrid scale (SGS) shear stress tensor and heat flux vector, respectively. The non-dimensional kinematic viscosity and thermal diffusivity are defined as $\nu = (Pr/(\Gamma^3 Ra))^{1/2}$ and $\kappa = 1/(\Gamma^3 RaPr)^{1/2}$, respectively.

The volume balance procedure by Schumann, Grötzbach & Kleiser (1979) is used for the integration over the fluid cells and the solution is evolved in time by means of the explicit Euler–Leapfrog scheme. Spatial derivatives and cell face velocities are approximated by piecewise integrated fourth-order accurate polynomials, where the velocity components are stored on staggered grids which are described in detail by Shishkina & Wagner (2007*a*). The velocity pressure coupling is performed through the projection method involving an elliptic solver by Swarztrauber (1974), where the

equations are decoupled in the homogeneous direction by means of a fast Fourier transform (FFT).

The flow field is initialized with a quiescent velocity field and the conduction profile for the temperature field. In order to be independent of numerical errors triggering convection after the initialization, small disturbances are superimposed onto the temperature field in order to excite instabilities. However, these disturbances are dissipated during the transient phase and do not have an effect once the solution is in equilibrium, i.e. heat transfer between hot and cold walls and turbulence intensity has reached a statistically steady state. Data for the statistical analysis is collected over a period of 110, 80, 70 and 40 non-dimensional time units for $Ra = 3.5 \times 10^5$, 3.5×10^6, 3.5×10^7 and 2.31×10^8, respectively.

In order to resolve the smallest relevant turbulent scales and the wall gradients in the DNS the resolution of the flow field must be sufficiently high. Therefore, the grid points are clustered in the vicinity of the walls using a hyperbolic tangential, so that about 10 grid points are within the thermal boundary layer and the grid spacing $h_{V_i} = (\Delta x\ \Delta y\ \Delta z)^{1/3}$ in the core region satisfies the Grötzbach (1983) estimate for the Kolmogorov scales η_k.

$$h_{V_i} \leqslant \eta_{k,Grö.} \equiv \frac{\pi}{\Gamma} \frac{\sqrt{Pr}}{((Nu-1)Ra)^{1/4}} \tag{2.2}$$

At the highest Rayleigh number the resolution in the core region of the domain is not high enough to resolve the Kolmogorov scales. In order to account for the SGS effects, the tensor diffusivity model by Leonard & Winkelmans (1999) is applied to top hat filtering (see Shishkina & Wagner 2007*a*),

$$\tau_{ij} \equiv \langle u_i' u_j' \rangle = \frac{1}{12} \sum_{j \neq k} (\Delta x_k)^2 \frac{\partial \langle u_i \rangle}{\partial x_k} \frac{\partial \langle u_j \rangle}{\partial x_k}, \tag{2.3}$$

$$h_i \equiv \langle u_i' \theta' \rangle = \frac{1}{12} \sum_{j \neq k} (\Delta x_k)^2 \frac{\partial \langle u_i \rangle}{\partial x_k} \frac{\partial \langle \theta \rangle}{\partial x_k}, \tag{2.4}$$

so that highly resolved large eddy simulations (LES) are performed for this Ra and for reasons of comparability an additional LES simulation is performed at $Ra = 3.5 \times 10^7$. Table 1 shows the mean Nusselt numbers averaged in time and over the top and bottom surfaces together with the Kolmogorov scales calculated from (2.2) and the grid spacing $h_{V_i,max}$ in the centre of the cell. It follows from table 1 that both LES are resolved equally well in the core region. However, no near-wall model needs to be employed, since the boundary layers are still well resolved. The numerical stability of the time-advancement scheme is more restrictive than the turbulent time scales of the flow, so the flows are well resolved temporally.

The resolution of the flow field is checked *a posteriori* by estimating the ratio of the mean cell size of each finite volume V_i and the smallest scales of the velocity and temperature fields, i.e. the Kolmogorov and Batchelor scales, respectively. These have to satisfy the relations

$$\frac{h_{V_i}}{\pi \eta_k(Ra, V_i)} \leqslant 1 \qquad \text{and} \qquad \frac{h_{V_i}}{\pi \eta_b(Ra, V_i)} \leqslant 1, \tag{2.5}$$

where $\eta_k(Ra, V_i) \equiv \nu^{3/4} / \overline{\epsilon_u'}^{1/4}$ and $\overline{\epsilon_u'}$ is the time-averaged turbulent kinetic dissipation rate and the Batchelor scales are defined analogously by $\eta_b(Ra, V_i) \equiv \kappa^{3/4} / \overline{\epsilon_\theta'}^{1/4}$ using the mean turbulent thermal dissipation rate $\overline{\epsilon_\theta'}$. Strictly this is valid only for

	3.5×10^5	3.5×10^6	3.5×10^7		2.31×10^8
Ra	DNS	DNS	DNS	LES	LES
Mesh size	$64 \times 128 \times 64$	$96 \times 256 \times 96$	$152 \times 512 \times 152$	$128 \times 256 \times 128$	$190 \times 512 \times 190$
Nu	6.225	12.12	22.87	23.38	40.62
δ_θ	7.81×10^{-2}	4.00×10^{-2}	2.05×10^{-2}	1.90×10^{-2}	1.11×10^{-2}
δ_u	1.12×10^{-1}	8.93×10^{-2}	7.14×10^{-2}	5.72×10^{-2}	4.92×10^{-2}
$\lvert\theta_e\rvert$	0.133	0.135	0.147	0.150	0.166
$\eta_{k,Grö.}$	7.17×10^{-2}	2.35×10^{-2}	1.58×10^{-2}	1.57×10^{-2}	8.57×10^{-3}
$\max(\eta_k)$	4.75×10^{-2}	2.32×10^{-2}	9.00×10^{-3}	9.19×10^{-3}	5.00×10^{-3}
$\max(\eta_b)$	2.25×10^{-2}	3.26×10^{-2}	1.76×10^{-2}	1.74×10^{-2}	1.15×10^{-2}
$h_{V_i,max}$	3.01×10^{-2}	1.72×10^{-2}	1.06×10^{-2}	1.50×10^{-2}	9.99×10^{-3}
$\max(h_{V_i}/\pi\eta_k)$	0.375	0.489	0.670	0.902	1.06
$\max(h_{V_i}/\pi\eta_b)$	0.226	0.312	0.464	0.631	0.773

TABLE 1. Results of the numerical simulations: mean viscous and thermal boundary layer thicknesses δ_u and δ_θ at $\hat{x}/\hat{W} = 0.5$, the temperature at the edge of the thermal boundary layer θ_e and the mean Nusselt number. Kolmogorov scales estimated with (2.2) and simulation results and the relative grid resolution is given for both the Kolmogorov and the Batchelor scales.

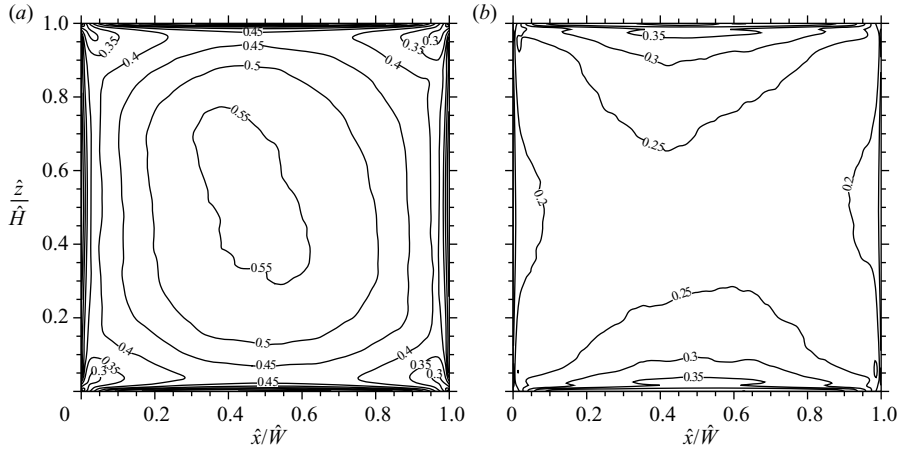

FIGURE 2. Ratio of the grid size compared to the (*a*) Kolmogorov and (*b*) Batchelor length scales for $Ra = 3.5 \times 10^7$ calculated *a posteriori* through (2.5).

homogeneous isotropic turbulence, however, we think this is a reasonable approach to obtain an indication of the resolution of the core region. Near the walls, where this criterion does not hold the requirement to resolve the gradients is usually much more restrictive. An example of the spatial resolution of the temperature and velocity fields is given by figure 2 for $Ra = 3.5 \times 10^7$ illustrating the sufficient resolution of the flow field. It can be seen that for this case in the core region the resolution of the velocity field is more critical than the temperature field. It is concluded that for $Pr = 0.7$ the temperature field dictates the resolution requirements near the walls and the velocity field in the core.

3. Interactions between temperature and velocity fields

Snapshots of the isosurfaces of the temperature fields are presented in figure 3. They illustrate the formation of the thermal plumes for the four Rayleigh numbers spanning

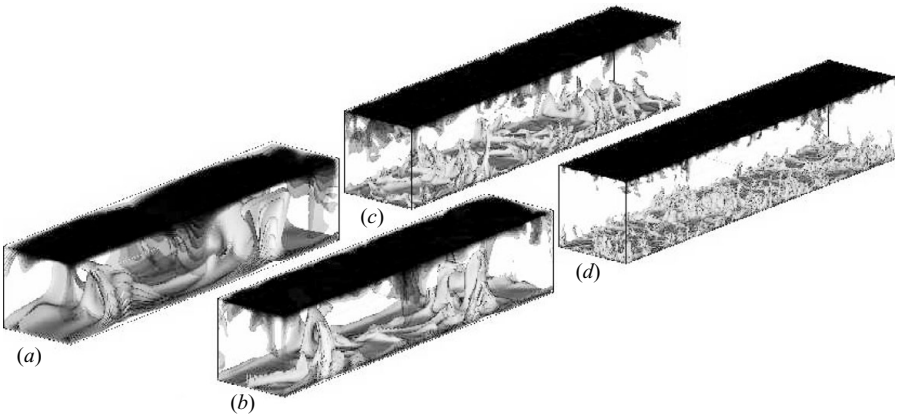

FIGURE 3. Snapshots of 16 instantaneous isotherms with $|\theta| \geqslant 0.1$: (*a*) $Ra = 3.5 \times 10^5$, (*b*) $Ra = 3.5 \times 10^6$, (*c*) $Ra = 3.5 \times 10^7$ and (*d*) $Ra = 2.31 \times 10^8$.

about four orders of magnitude from the onset of turbulence until a fully developed or hard turbulent flow field is reached (see Castaing *et al.* 1989). At the lowest Ra two pairs of plumes are rising and falling, and hence forming the typical convection rolls with their rotational axes orthogonal to the longitudinal direction of the cell. At $Ra = 3.5 \times 10^7$ the flow field becomes fully turbulent and many small plumes can be observed. The interaction of the thermal plumes still causes a large scale circulation of the flow. However, at this Rayleigh number the large-scale convection rolls are not continuously maintained, but appear to become unstable, which temporarily leads to a breakdown of the large-scale flow. At $Ra = 2.31 \times 10^8$ the temperature field is entirely dominated by small-scale structures, so that a large-scale convection roll can hardly be identified in the temperature field. This phenomenon will be discussed in detail in § 3.3. In § 3.2, the boundary layer thicknesses are discussed and results are provided by table 1.

3.1. *Thermal and viscous dissipation rate analysis*

A horizontal and a vertical cut through the centre of the cell illustrate the distribution of the turbulent kinetic and thermal dissipation rates, $\overline{\epsilon'_u}$ and $\overline{\epsilon'_\theta}$, shown in figure 4(*a–d*). The turbulent kinetic dissipation rate is almost constant in the core and increases gradually within the boundary layer where viscosity effects come to bear. The turbulent thermal dissipation rates, however, reflect a much more complex three-dimensional variation which is also dependent on Ra. A plateau begins to form in the core region as Ra increases indicating that in the core heat is dissipated more equally at higher Rayleigh numbers. A local minimum of $\overline{\epsilon'_\theta}$ is observed at the edge of the thermal boundary layer, whereas a local maximum is found at the edge of the viscous boundary layer of the sidewalls. Both local extrema are vanishing with increasing Ra. Comparison of the kinetic and thermal turbulent dissipation rates reveals that the latter are significantly smaller throughout the flow field, which could not be expected for the considered fluid of $Pr = 0.7$. For a more detailed analysis the ratio of both dissipation rates $\overline{(\partial u'/\partial x_i)^2}/\overline{(\partial \theta'/\partial x_i)^2}$ is investigated. Figures 4(*e*) and 4(*f*) reveal that this ratio is greater than one in the bulk, but reduces towards the walls. In the core region this ratio is increasing from approximately 7.5 to 20 from the lowest to the highest simulated Rayleigh number which indicates that velocity fluctuations are always dominant in this region. However, a minimum is found near

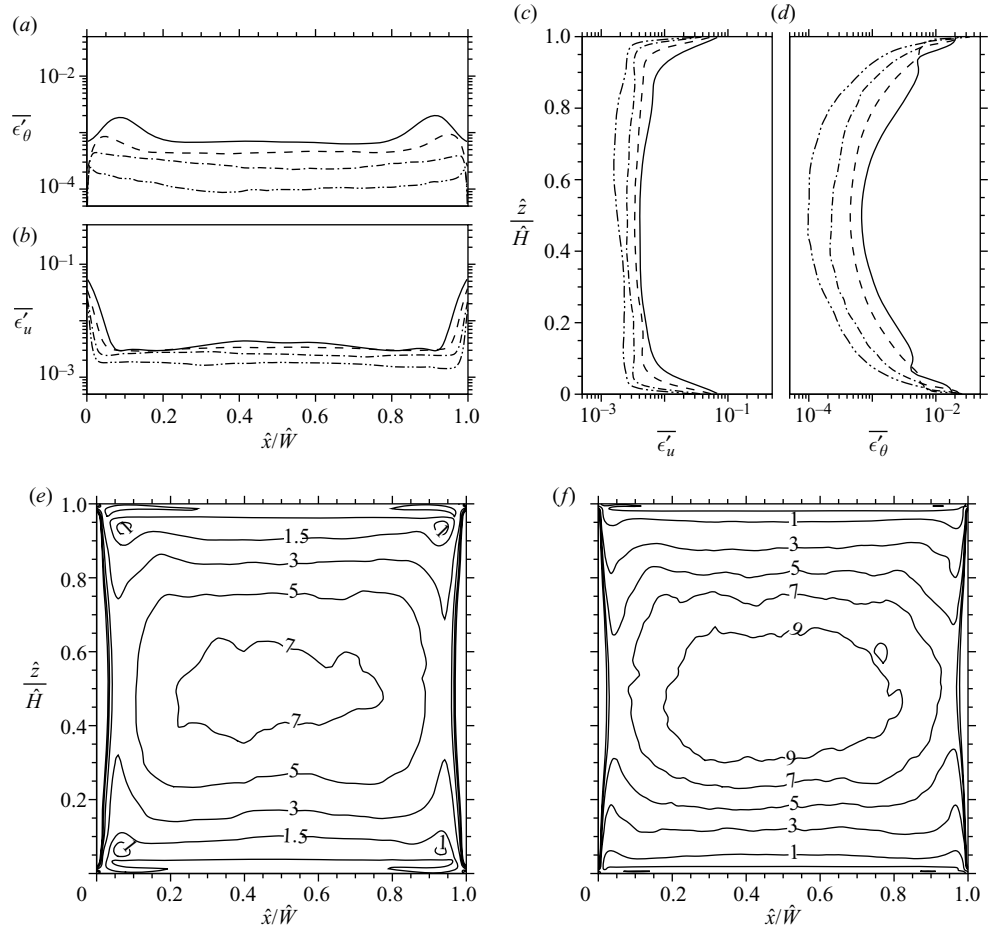

FIGURE 4. Temporally averaged turbulent kinetic dissipation rates $\overline{\epsilon'_u}$ (*b*, *c*) and thermal dissipation rates $\overline{\epsilon'_\theta}$ (*a*, *d*) in the centre planes $\hat{z}/\hat{H}=0.5$ (*a*, *b*) and $\hat{x}/\hat{W}=0.5$ (*c*, *d*) for $Ra=3.5\times10^5$ (—), $Ra=3.5\times10^6$ (– –), $Ra=3.5\times10^7$ (–·–) and $Ra=2.31\times10^8$ (–··–). Ratio of $\overline{(\partial u'/\partial x_i)^2}/\overline{(\partial\theta'/\partial x_i)^2}$ for two Rayleigh numbers: $Ra=3.5\times10^5$ (*e*) and $Ra=3.5\times10^7$ (*f*).

the edge of the thermal boundary layer reflecting strong interactions between velocity and temperature fluctuations. It is noted that the minimum of $\overline{(\partial u'/\partial x_i)^2}/\overline{(\partial\theta'/\partial x_i)^2}$ decreases to approximately one as Ra increases. This means that dissipation of turbulent thermal energy becomes increasingly intense in the boundary layers as Ra increases, whereas turbulent kinetic dissipation dominates the core.

3.2. *Boundary-layer thicknesses*

In figure 5 the profiles of the mean and r.m.s. values of temperature (averaged in time and periodic direction) are plotted for the centre plane ($\hat{x}/\hat{W}=0.5$) of the cell. The typical natural convection temperature profile is found with a mean temperature gradient in the bulk close to zero. We consider the small deviations from the zero gradient and the arithmetic mean temperature of the top and bottom plates in this region to be a result of the finite averaging time our numerical simulations are bound to. The corresponding r.m.s. values clearly illustrate the decreasing thickness of the

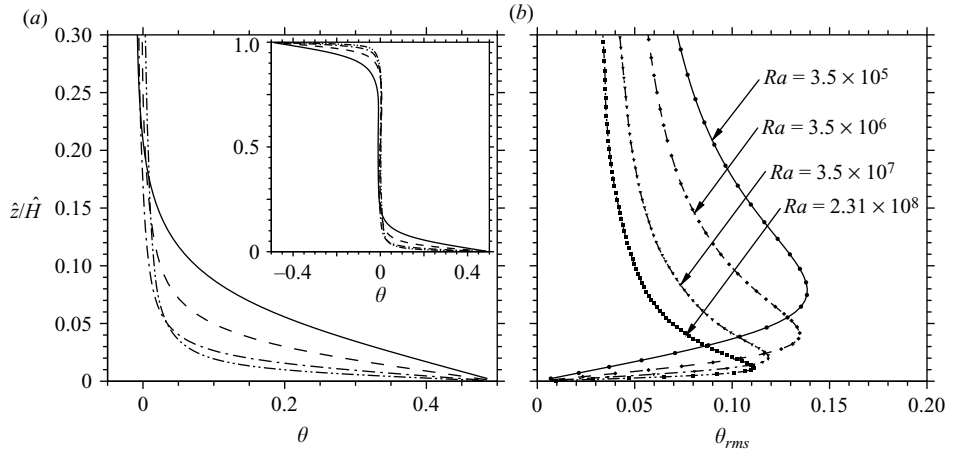

FIGURE 5. (*a*) Mean temperature profiles and (*b*) corresponding r.m.s. values of temperature extracted at $\hat{x}/\hat{W} = 0.5$ for $Ra = 3.5 \times 10^5$ (—), $Ra = 3.5 \times 10^6$ (– –), $Ra = 3.5 \times 10^7$ (–·–) and $Ra = 2.31 \times 10^8$ (–··–).

boundary layer as Ra increases. The close-up view of the r.m.s. profiles shows that the thermal boundary layer is well resolved with about 10 grid points. Essentially by definition the r.m.s. values must vanish towards the isothermal walls to comply with the boundary conditions as pointed out by Verzicco & Sreenivasan (2008).

The viscous and thermal boundary layer thicknesses δ_u and δ_θ are determined through the maximum r.m.s. value criterion (see e.g. Belmonte, Tilgner & Libchaber 1994) in the centre of the cell ($\hat{x}/\hat{W} = 0.5$). The extracted boundary layer thicknesses are specified in table 1. The thermal boundary layer thickness is found to scale with $\delta_\theta \sim Ra^{-0.291}$. Given that $Nu = 1/(2\delta_\theta)$ this result matches well with the observation and theoretical prediction of Castaing *et al.* (1989) and the theoretical prediction of Grossmann & Lohse (2004). It is also observed that the LES results do not yield the same boundary layer thicknesses, but the Ra dependencies are very well extended to higher Ra. Further figure 6 compares the results of the present study to data by Hartlep, Tilgner & Busse (2005) obtained through DNS in a thin fluid layer. The scaling $\delta_\theta \sim Ra^{-0.291}$ is given for reference and the thermal boundary layer thicknesses are also plotted in compensated form in order to illustrate the good description of the data by the least squares fit. The figure clearly shows the good agreement between the two simulations, in particular for the thermal boundary layer thicknesses. Hartlep (2004) found an exponent $\beta = 0.278$ for the scaling of the thermal boundary layer and a slightly thinner viscous boundary layer. We consider these small discrepancies to be effects of the additional lateral walls of the rectangular cell. It can be seen that in both simulations the thicknesses of viscous and thermal boundary layers decrease at different rates, which was also found through the DNS of Verzicco & Camussi (2003*a*) in a slender cylindrical cell and was theoretically predicted by Grossmann & Lohse (2000, 2004).

3.3. *Analysis of the turbulent fluctuations*

Energy spectra of the velocity and temperature fields extracted from the periodic direction and averaged in time are plotted in figure 7 for various wall distances for three Ra revealing clear differences between the velocity and temperature fields. Velocity spectra (*a*,*b*,*c*) approach the $-5/3$ power of the Kolmogorov-law (see

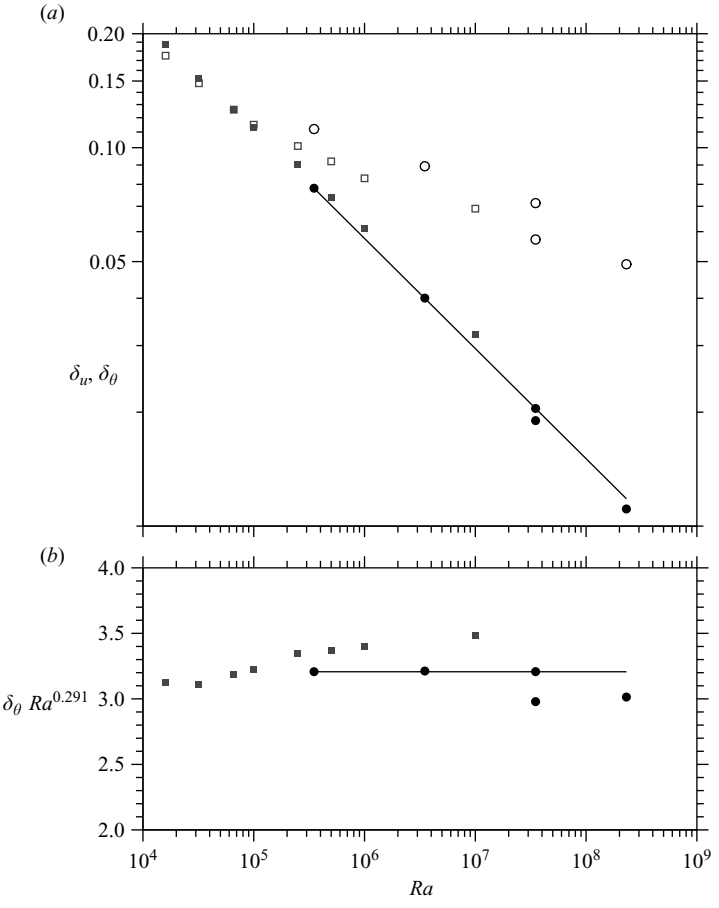

FIGURE 6. Thermal and viscous boundary layer thicknesses δ_θ (closed symbols) and δ_u (open symbols). Circles correspond to the presented simulations extracted at $\hat{x}/\hat{W} = 0.5$ and squares to DNS simulations of an infinitely extended fluid layer by Hartlep (2004); The scaling $Nu \sim Ra^{-0.291}$ is given for reference (—). Any horizontal trace in (*b*) is consistent with the scaling exponent $\beta = 0.291$.

Oboukhov 1962) towards the centre of the cell which is indicated by the power law fits and increasing wall distance is indicated by the arrows. Plots (*d*,*e*,*f*), however, show a $-7/5$ decrease in the equilibrium range, the so called Bolgiano (1959) scaling, which is in agreement with findings by Verzicco & Camussi (2003*a*) and Lohse (1994).

At the lowest Rayleigh number energy spectra of the velocity and temperature fields show a distinct peak in the cell centre ($\hat{z}/\hat{H} = 0.5$ and $\hat{x}/\hat{W} = 0.5$, indicated by the power-law fits) for the wavenumber $k = 2$. This is due to the fact that a convective pattern is formed in a way that two pairs of convection rolls are established. However, as Ra increases the peak at $k = 2$ is vanishing in the temperature spectra and a second peak begins to form at $k = 4$ which is of similar strength as the one at $k = 2$. This indicates that the large-scale plumes begin to vanish and the flow is dominated by increasingly smaller structures. Since temperature and velocity fields behave differently in the bulk for $Ra \geqslant 3.5 \times 10^7$, it is concluded that both fields begin to decorrelate as far as the dominant structures of the flow fields are concerned once a fully

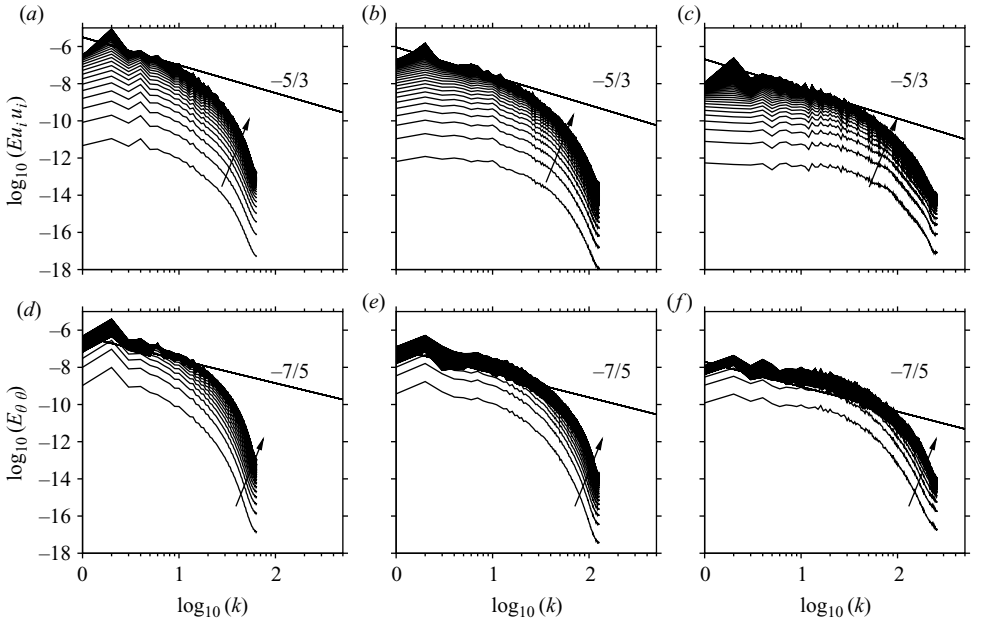

FIGURE 7. Kinetic (a, b, c) and thermal energy spectra (d, e, f) recorded at $\hat{x}/\hat{W} = 0.5$ for all grid points with $\hat{z}/\hat{H} \leqslant 0.5$; ($a$, d) $Ra = 3.5 \times 10^5$, (b, e) $Ra = 3.5 \times 10^6$ and (c, f) $Ra = 3.5 \times 10^7$. Arrows indicate increasing wall distance; the position of the power-law fit indicates the centre of the cell.

developed turbulent flow is achieved. However, it is noticed that the thermal plumes, independently of their size, maintain the large-scale convection rolls.

It is also noted that the thermal energy is not continuously increasing towards the cell centre as observed for the velocity field. This is investigated in more detail by analysing the energy of the temperature field $E_{\theta\theta}$ and the velocity field $E_{u_iu_i}$ held by one particular wavenumber k, which is plotted in figure 8(a) for an arbitrarily chosen $k = 8$ as a function of vertical wall distance at mid-span of the cell ($\hat{x}/\hat{W} = 0.5$). It illustrates that turbulent kinetic energy is increasing towards the centre of the cell. However, it is observed that outside the thermal boundary layer, but still inside the viscous one, a kink is formed before it increases further. The kinks coincide with the minimum of $\overline{(\partial u'/\partial x_i)^2}/\overline{(\partial\theta'/\partial x_i)^2}$ discussed in § 3.1. The temperature spectra on the other hand show a distinct maximum at the edge of the thermal boundary layer, which becomes increasingly pronounced as Ra increases and the level of turbulent thermal energy held by one wavenumber is steadily decreasing towards the centre. This indicates that there are strong interactions between both fields at the edge of the thermal boundary layer emanating from the thermal plumes, since this behaviour is not observed at the adiabatic walls illustrated in figure 8(b), where only a viscous boundary layer is formed and the turbulent thermal fluctuations are independent of the horizontal position. It is therefore concluded that the thermal plumes which are ejected from the thermal boundary layers transform thermal energy into kinetic energy. Consequently, the velocity field is still gaining turbulent kinetic energy outside the boundary layers as the fluid is convected towards the opposite conducting wall, whereas the temperature field loses thermal energy. This is consistent with the conclusions drawn by Xi, Lam & Xia (2004) who argued that the thermal

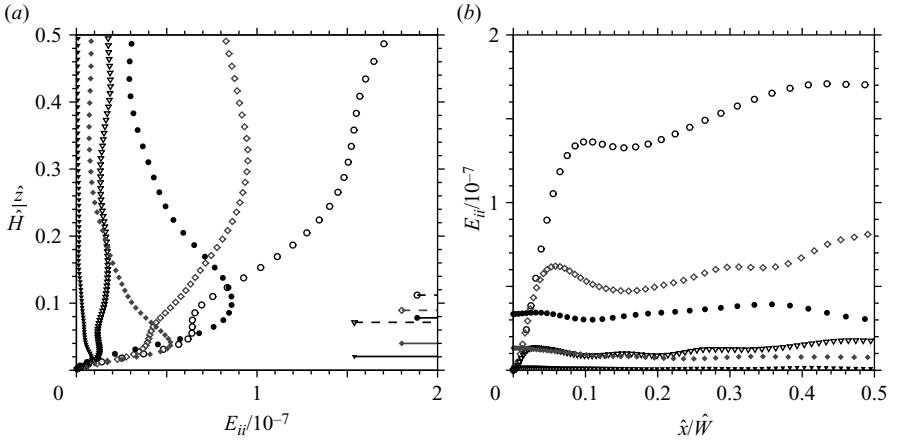

FIGURE 8. Turbulent energy of velocity (open symbols) and temperature (closed symbols) as a function of wall distance. Plotted is wave-number $k = 8$ recorded between the vertical walls at $\hat{x}/\hat{W} = 0.5$ (a) and between the horizontal walls at $\hat{z}/\hat{H} = 0.5$ (b). $Ra = 3.5 \times 10^5$ ($\bigcirc$), $Ra = 3.5 \times 10^6$ ($\diamond$) and $Ra = 3.5 \times 10^7$ (∇); horizontal lines indicate the temporal mean of the edge of the thermal (—) and the viscous (– –) boundary layers.

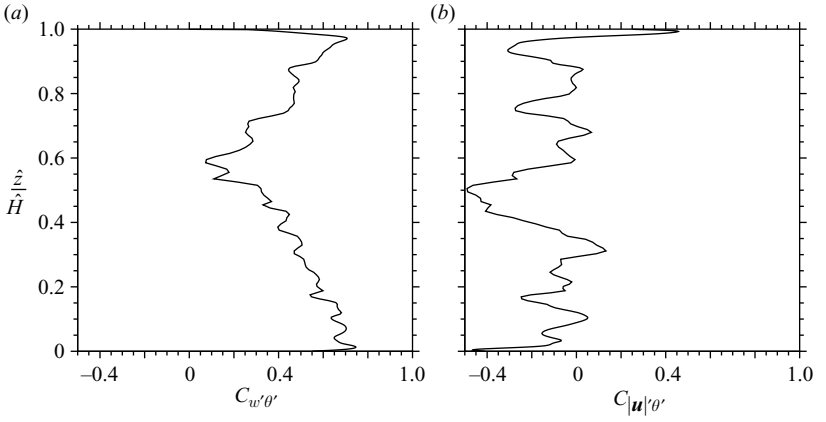

FIGURE 9. Correlation coefficient of the turbulent fluctuations of the velocity and temperature fields at a single longitudinal position for $Ra = 2.31 \times 10^8$ based on (a) the vertical velocity fluctuations $C_{w'\theta'}$ and (b) the fluctuations of the velocity magnitude $C_{|\boldsymbol{u}|'\theta'}$.

plumes generate vortices as they propagate towards the opposite plate, and hence feed kinetic energy into the flow field.

The correlation coefficient $C_{w'\theta'} = \overline{w'\theta'}/\sqrt{\overline{w'^2}\,\overline{\theta'^2}}$ is calculated at one position midway between the lateral walls. Figure 9(a) clearly shows that the correlation between the turbulent fluctuations of the temperature and vertical velocity fields decreases from about 0.8 near the conducting walls to almost 0 in the centre. The correlation coefficient based on the fluctuations of the velocity magnitude $|\boldsymbol{u}|'$ illustrates nicely that both turbulent fields are strongly coupled within the boundary layers and are only weakly (anti-)correlated in the core region. However, we think this is overestimated due to very small turbulent fluctuations in the core, since the correlation $|\boldsymbol{u}|'\theta'$ does not yield such a strong anti-correlation.

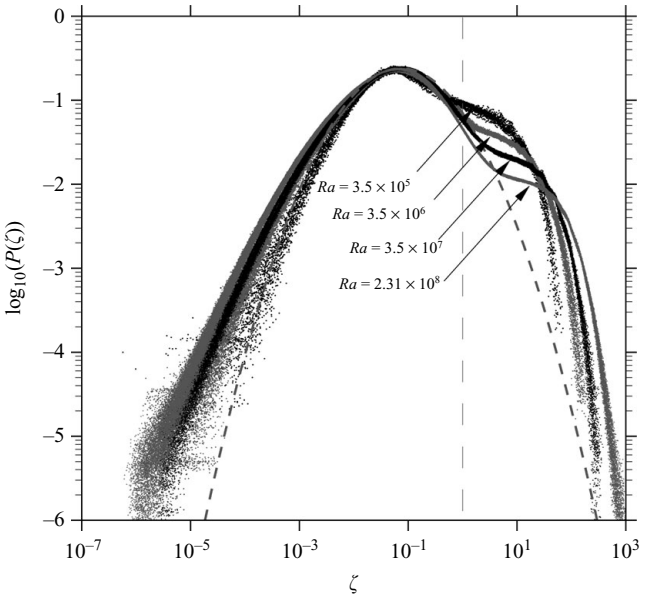

FIGURE 10. PDFs of the thermal dissipation rates; the vertical dashed line indicates the volume-averaged thermal dissipation rate, a Gaussian distribution (- - -), where the mean is chosen to fit the maximum of $P(\zeta)$, is given for reference.

4. Thermal dissipation rate analysis

In order to investigate the thermal dissipation rates and the contribution of different features of the flow field to the heat transfer their probability density functions (PDFs) have been evaluated using an exponential bin width $\Delta(n) \sim (\zeta_{max}/\zeta_{min})^{n/500}$, for $n = 1, \ldots, 500$ and the ratio between the highest and the lowest normalized thermal dissipation rates $\zeta_{max}/\zeta_{min} = 10^8$. Here $\zeta = \epsilon_\theta / \langle \epsilon_\theta \rangle_V$ is a thermal dissipation rate normalized with the volume-averaged mean and $P(\zeta)$ denotes its probability.

Figure 10 shows the PDFs of the thermal dissipation rates that have been calculated from instantaneous flow fields. We associate thermal dissipation rates with $\zeta \gg 1$ with the temperature gradients in the vicinity of the conducting walls and $\zeta \ll 1$ with the bulk flow where temperature fluctuations dominate over dissipation rates due to the low-mean gradient.

Due to intermittency effects the tails deviate increasingly from the Gaussian distribution at high Ra. Figure 10 also shows that the Gaussian distribution falls below $P(\zeta)$ for $\zeta \ll 1$, which is in agreement with observations for passive scalars by Schumacher & Sreenivasan (2005). The differences compared to the passive scalar convection PDFs for $\zeta > 1$ are therefore considered to be a result of the thermal plumes and boundary layers. It can be seen that the PDFs have very similar tails and a maximum that becomes increasingly pronounced with a gradient around $\zeta \approx 1$ that steepens significantly as Ra increases. This indicates that at high Rayleigh numbers a distinct separation between high and low thermal dissipation rates occurs.

The shape of the PDFs and their behaviour with increasing Ra further suggests that the thermal dissipation rates can be divided into three regions. In order to separate small and large thermal dissipation rates, the two inflection points of the

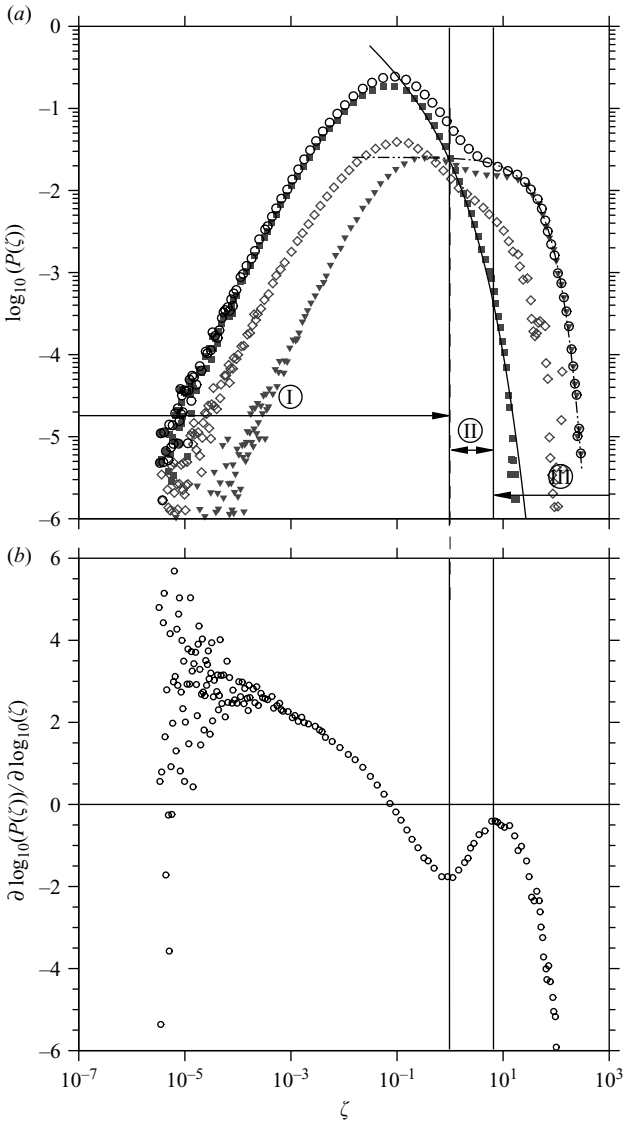

FIGURE 11. (*a*) Example of a thermal dissipation rate distribution derived from $Ra = 3.5 \times 10^7$ data showing the overall PDF (○) and the contributions from the three subdomains: region *a* core: (■), which can be approximated with a stretched exponential (—), region *b* conductive sublayer: (▼) and the exponential fit (– · –) and region *c* intermediate layer: ◇. (*b*) Local slope of the same PDF illustrating the definition of the limits of region I which is the bulk-turbulence-dominated region and region III which is the conduction-dominated region. The intermediate regime II is associated with the thermal plumes and outer boundary layers.

PDF are taken to distinguish between the three regions as indicated by the sample PDF shown in figure 11. Following the above assumption, the regions represent

I the bulk flow,

II the plumes/mixing layers and

III the conductive sublayers,

and hence are associated, respectively, with parts of the flow that are dominated by passive scalar convection (since there are no significant temperature differences),

	3.5×10^5	3.5×10^6	3.5×10^7		2.31×10^8
Ra	DNS	DNS	DNS	LES	LES
$\zeta_{(P_{max})}$	4.67×10^{-2}	5.91×10^{-2}	7.38×10^{-2}	7.57×10^{-2}	6.30×10^{-2}
ζ_{I-II}	0.169	0.495	0.971	0.887	0.978
ζ_{II-III}	0.879	3.16	6.56	7.47	11.5
A_1	1.806×10^{-1}	1.884×10^{-1}	1.672×10^{-1}	4.017×10^{-1}	4.294×10^{-1}
A_2	3.915	2.464	1.998	2.879	2.967
α	1.034	0.993	0.993	0.838	0.752
B_1	7.089×10^{-2}	3.587×10^{-2}	2.544×10^{-2}	2.354×10^{-2}	0.952×10^{-2}
B_2	8.536×10^{-2}	4.419×10^{-2}	2.890×10^{-2}	2.712×10^{-2}	1.263×10^{-2}
σ	16.22	16.76	16.98	16.87	19.13
S	−0.250	−0.248	−0.245	−0.247	−0.257
K	−2.926	−2.924	−2.925	−2.925	−2.924
σ_a	12.77	14.90	15.16	15.21	17.41
S_a	−0.355	−0.303	−0.295	−0.291	−0.291
K_a	−2.862	−2.900	−2.902	−2.905	−2.906
σ_b	7.821	4.898	4.191	3.057	2.136
S_b	−0.384	−0.265	−0.045	0.483	0.864
K_b	−2.768	−2.524	−2.351	−1.915	−0.778

TABLE 2. Location of the maximum and inflection points of the PDFs as a function of Ra, the coefficients B_1 and B_2 of the least-squares fit obtained through (4.1) and the coefficients A_1, A_2 and α of (4.2) obtained through a least-squares fit of the ensemble data set for $\zeta_{limit} > 10\ \zeta_{(P_{max})}$. Standard deviation σ, skewness S and kurtosis K of the thermal dissipation rate PDFs.

turbulent mixing and conduction at the walls (where the strongest gradients are found).

The thermal dissipation rates associated with the inflection points and the maximum contribution are given in table 2. Both inflection points are moving towards higher thermal dissipation rates and the range of dissipation rates between these points increases. In order to support the above approach of the separation of the thermal dissipation rates, PDFs are calculated not only for the entire volume but also for specific parts of the flow field. Here, plumes and boundary layers are thought to be fluid with $|\theta| > |\theta_e|$, where θ_e is the temperature at the edge of the thermal boundary layer specified by table 1. Consequently contributions from this region should equal those of regions II and III together. In contrast to the previous approach, where the bulk flow was defined as the region containing only small ζ, we now evaluate the core region of the flow by cutting a cubic subdomain out of the centre of the cell. The boundaries of this box are defined to be just outside the mean viscous and thermal boundary layers specified in table 1. However, fluid with $|\theta| > |\theta_e|$ is neglected during the evaluation of the core region. Hence, one obtains three regions

(*a*) core without $|\theta| > |\theta_e|$ fluid,

(*b*) boundary layers and plumes ($|\theta| > |\theta_e|$),

(*c*) intermediate layer (remainder),

whose sum yields the overall PDF again. It is also worth pointing out that we intentionally distinguish between the bulk, i.e. region I, which by definition contains only small thermal dissipation rates, and the core, i.e. region *a* which is mainly geometrically defined.

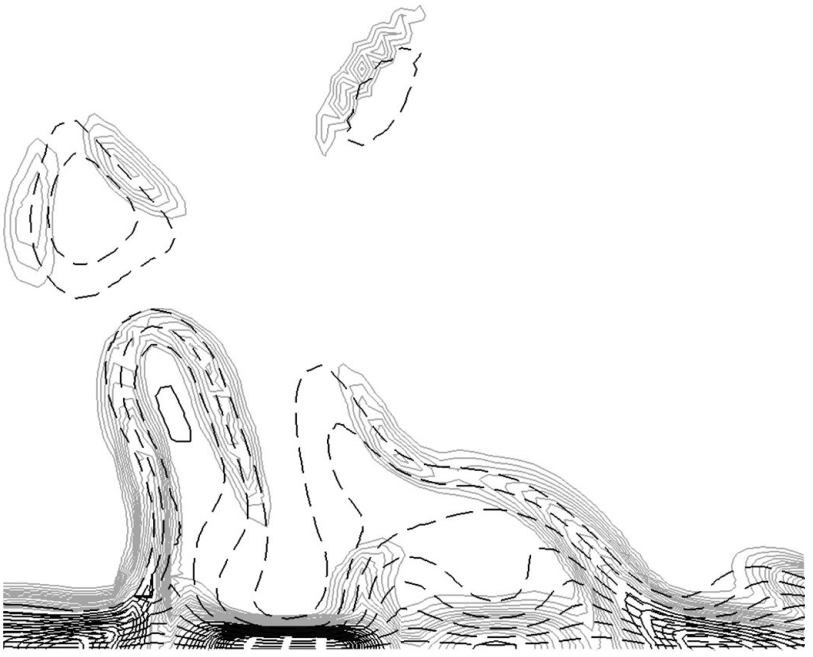

FIGURE 12. Close-up view of the thermal dissipation rate distribution in a vertical section through the cell. Isolines in dark grey represent thermal dissipation rates of regime III and light grey isolines represent those of regime II. Isothermal lines (– –) with $0.1 \leqslant |\theta| \leqslant 0.45$ are given for reference; $Ra = 3.5 \times 10^7$.

The sample PDFs illustrated in figure 11 highlights that the tails of region *a* and region I largely coincide, but region *a* also contains larger thermal dissipation rates. Comparing the contributions of regions *a*–*c* to the small ζ contributions of the overall PDF, i.e. region I, we conclude that the core region *a* is a subset of the bulk I. By definition the latter extends to the sidewalls, so that regions *a* and *c* should show the same tendencies as region I. Similar result is found for regions *b* and III, whose tails are almost identical. Region II on the other hand is dominated by contributions from *b*, but core and intermediate layers still have a significant influence on this region, which to some extent are effects of entrainment due to the thermal plumes. Therefore we refer to region II as the plume and mixing layer dominated region.

This region separates the bulk flow I from the conductive sublayer III. In order to illustrate the spatial distribution of the thermal dissipation rates of regions II and III isolines of their dissipation rates are plotted in figure 12 together with isolines of temperature. It can be seen that dissipation rates of region III (shown in dark grey) correspond to regions where the isothermal lines are almost parallel indicating that this region is conduction-dominated. Furthermore, the intermediate region II is found to correlate rather well with the mixing layers and thermal plumes rising (or falling) from the hot (or cold) walls, whereas region I contributions are mainly found in the bulk.

From the above definitions of the bulk flow, the plumes and the conductive sublayer the respective contributions of these features can be estimated. The results of this approach will be further discussed in § 4.3.

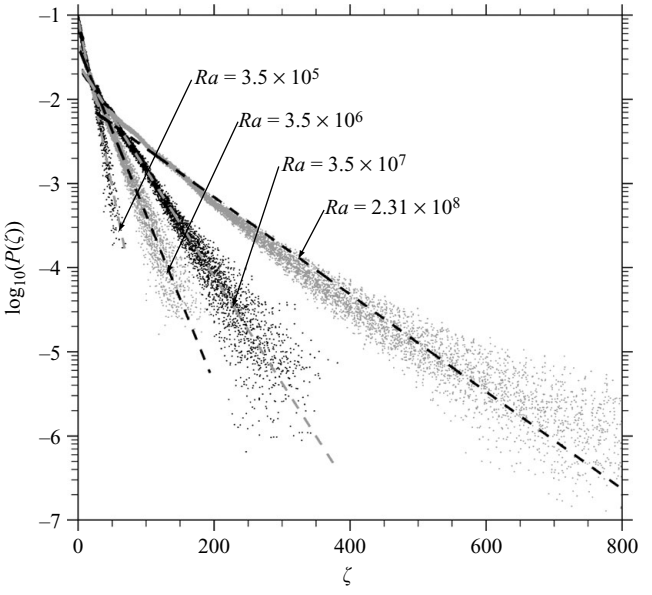

FIGURE 13. PDFs of the time series of region III for the thermal dissipation rates associated with the conductive sublayer are shown together with least-squares fits (– – –).

4.1. *Thermal dissipation rates in the boundary layers*

From the statistically averaged temperature profile the mean temperature at the edge of the thermal boundary layer θ_e is taken to separate the thermal boundary layers and plumes, which are considered to contain fluid with $|\theta| > |\theta_e|$. However, this criterion is based on averaged quantities and is applied to instantaneous flow fields and therefore not sufficient to separate the instantaneous thermal boundary layers from the effects of turbulent intermittency in the bulk. This results in a cross-over region of the dissipation rates $\zeta \approx 1$ associated with regions *a* and *b* as indicated by figure 11. Nonetheless this analysis underlines that very high thermal dissipation rates are primarily found in the near-wall region. It could be concluded that high thermal dissipation rates are due to the mean temperature gradients near the walls, but figure 4(*d*) shows that the fluctuations of the thermal dissipation rate increase in the vicinity of the conducting walls and decrease only in the outer boundary layers (which we refer to as the mixing layers) and the core.

Furthermore region *b* largely coincides with region III and follows an exponential scaling of the form

$$P(\zeta \gg 1) = B_1 \exp(-B_2\,\zeta). \tag{4.1}$$

PDFs are calculated for the region *b* over a long period of time. The coefficients of (4.1) are determined for the ensemble average of $\zeta > 2\ \zeta_{II-III}$. The data and the corresponding least-squares fits are shown in figure 13. Since the exponent B_2 of the right tail becomes smaller, it is concluded that with increasing *Ra* a broader range of dissipation rates becomes important. This is in agreement with observations detailed at the beginning of § 4.

Time series of B_2 is provided in figure 14. They show an oscillating behaviour of the exponent for all Rayleigh numbers, which is associated with the shedding of the plumes from the boundary layers. During the ejection of a plume fluid of high

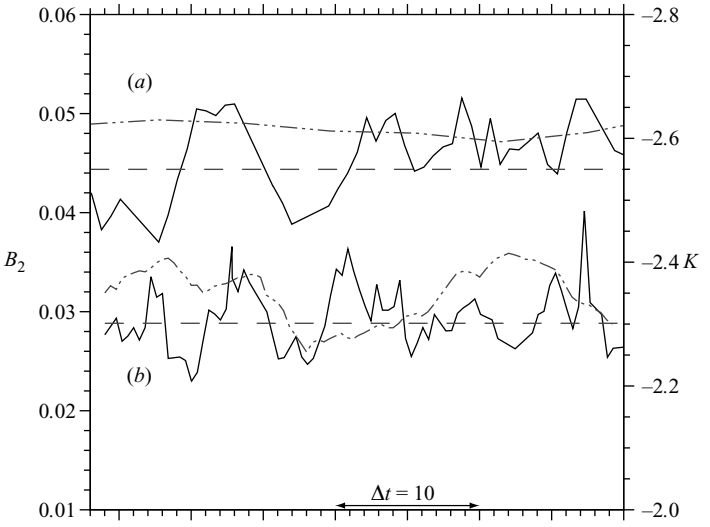

FIGURE 14. Time series of the exponent B_2 (—) of (4.1) and the kurtosis of the PDF of region b (– · · –) for (a) $Ra = 3.5 \times 10^6$ and (b) $Ra = 3.5 \times 10^7$. The dashed lines indicate the ensemble average given by table 2.

ϵ_θ is convected away from the wall, leading to a smaller probability of high thermal dissipation rates, and thus larger B_2. It can be seen that with increasing Ra the frequency of the plume ejection increases, indicating that smaller plumes are ejected more rapidly. The shedding period T_{shed} obtained from the time series for $Ra = 3.5 \times 10^6$ and $Ra = 3.5 \times 10^7$ are $T_{shed} \approx 9.7$ and $T_{shed} \approx 5.6$, respectively. However, it is noted that the time series of the kurtosis $K = (\sum_i \log(\zeta_i)^4 P(\zeta_i))/(\sum_i \log(\zeta_i)^2 P(\zeta_i)) - 3$ of the PDFs calculated from region b are significantly smoother, but still reflect an increasingly unsteady behaviour. It is also observed that K is increasing from approximately -3 to -0.8 between $Ra = 3.5 \times 10^5$ and 2.31×10^8 with the largest change of K occurring between $Ra = 3.5 \times 10^7$ and 2.31×10^8 (see table 2). This reveals that the thermal boundary layers change dramatically when a fully developed temperature field is achieved. Furthermore, comparison of the statistical moments of the PDFs given by table 2 emphasizes that the boundary layers of the LES are most affected by the reduced resolution of the core region. It can be seen that the core region PDFs are almost identical, for the DNS and LES results at $Ra = 3.5 \times 10^7$, but those of the boundary layers differ significantly.

4.2. *Thermal dissipation rates in the core*

The PDFs obtained in the core region a of the flow field are provided by figure 15. Comparison with region III of the overall PDFs reveals that most of the small ζ contributions of figure 10 are due to the core region. The detailed view of this region shows a picture similar to the results obtained in passive scalar convection (see Schumacher & Sreenivasan 2005); the probability density functions of the thermal dissipation rates are neither symmetric nor Gaussian. For very small ζ the Gaussian function falls below the PDFs, reflecting strong intermittency effects of the small scales. The right tail was fitted with a stretched exponential function for $\zeta > 10\ \zeta_{(P_{max})}$

$$P(\zeta > 10\ \zeta_{(P_{max})}) = \frac{A_1}{\sqrt{\zeta}} \exp(-A_2\ \zeta^{\alpha/2}), \tag{4.2}$$

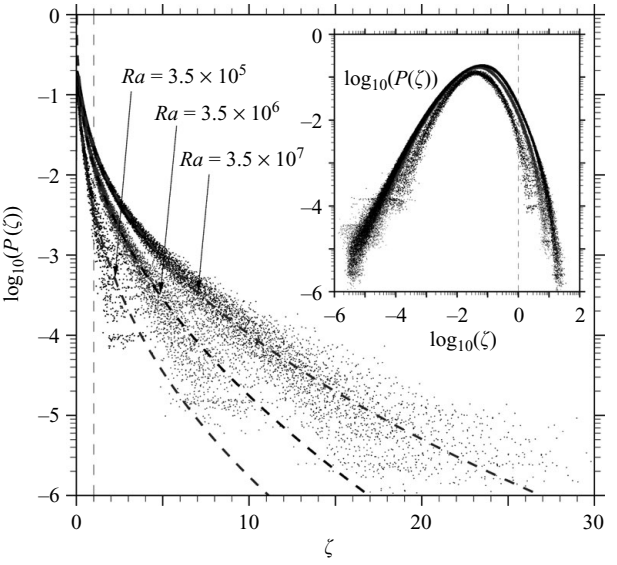

FIGURE 15. PDFs of the core region (a) with their respective least-squares fits (– – –); the vertical dashed line indicates the mean thermal dissipation rate. The inset shows the same PDFs on a log–log scale to illustrate the distribution of the small thermal dissipation rates.

which was analytically derived for passive scalar turbulence in the limit of large Pr and Peclét numbers by Chertkov, Falkovich & Kolokolov (1998) and Gamba & Kolokolov (1999) who found $\alpha = 2/3$. The coefficients obtained through least-squares fits of the ensemble average are given in table 2. It is observed that the coefficients A_1 and A_2 seem to have a minimum around $Ra \approx 10^7$, whereas $\alpha \approx 1$ is found for $Ra \lesssim 10^7$ and it seems to be decreasing once the flow has become fully turbulent. Thus there seems to be a tendency for α to approach the theoretically predicted passive scalar scaling at high Ra. As for the overall PDFs it is found that intermittency effects of the tails are increasing and the maximum of the function is shifted towards the volume-averaged dissipation rate for $Ra < 3.5 \times 10^7$ and moves towards smaller ζ again at $Ra = 2.31 \times 10^8$. This behaviour reflects that the flow field undergoes a significant change from developing (soft) turbulence at $Ra < 3.5 \times 10^7$ to a fully developed turbulent temperature field at $Ra = 2.31 \times 10^8$, when the shape of the PDF's right tail begins to change from an exponential to a stretched exponential function as can be seen from table 2. Thus in the core region two important effects are observed: a continuous decrease of $\overline{\epsilon'_\theta}$ and a change of the PDF's tail once the temperature field has become fully turbulent.

Time series of the parameters A_2 and α obtained through least-square fits of the respective instantaneous flow shows that the exponent α is fluctuating with noticeable spikes representing rare but extreme events. This is also reflected by the temporal behaviour of the kurtosis K of the core region PDFs calculated from the instantaneous flow fields. Figure 16 illustrates that the ensemble average of K decreases with Ra, i.e. the PDFs of the core region become flatter, but it is also observed that there are noticeable spikes of relatively high K. This reveals that a broad range of thermal dissipation rates becomes more equally distributed in the core region as Ra increases and the flow is rarely disturbed by the thermal plumes.

Ra	3.5×10^5 DNS	3.5×10^6 DNS	3.5×10^7 DNS	3.5×10^7 LES	2.31×10^8 LES
core $\langle\epsilon_\theta\rangle_a/\langle\epsilon_\theta\rangle_V$	0.04 (0.04)	0.08 (0.07)	0.11 (0.11)	0.10 (0.10)	0.10 (0.10)
bl and *pl* $\langle\epsilon_\theta\rangle_b/\langle\epsilon_\theta\rangle_V$	0.75 (0.29)	0.76 (0.29)	0.70 (0.28)	0.71 (0.28)	0.67 (0.27)
intermediate $\langle\epsilon_\theta\rangle_c/\langle\epsilon_\theta\rangle_V$	0.21 (0.10)	0.16 (0.09)	0.19 (0.11)	0.19 (0.11)	0.22 (0.14)
bulk $\langle\epsilon\rangle_{\mathrm{I}}/\langle\epsilon_\theta\rangle_V$	0.12 (0.03)	0.11 (0.06)	0.12 (0.10)	0.12 (0.10)	0.10 (0.07)
pl and mixing layers $\langle\epsilon\rangle_{\mathrm{II}}/\langle\epsilon_\theta\rangle_V$	0.54 (0.32)	0.67 (0.30)	0.73 (0.27)	0.74 (0.25)	0.75 (0.17)
conductive sublayer $\langle\epsilon\rangle_{\mathrm{III}}/\langle\epsilon_\theta\rangle_V$	0.34 (0.06)	0.22 (0.09)	0.15 (0.11)	0.14 (0.10)	0.15 (0.06)

TABLE 3. Contributions of regions *a* to *c* (top) and regions I to III (bottom) to the volume averaged thermal dissipation rate. Values in brackets specify the contributions of the turbulent fluctuations to the contributions of the volume-averaged mean.

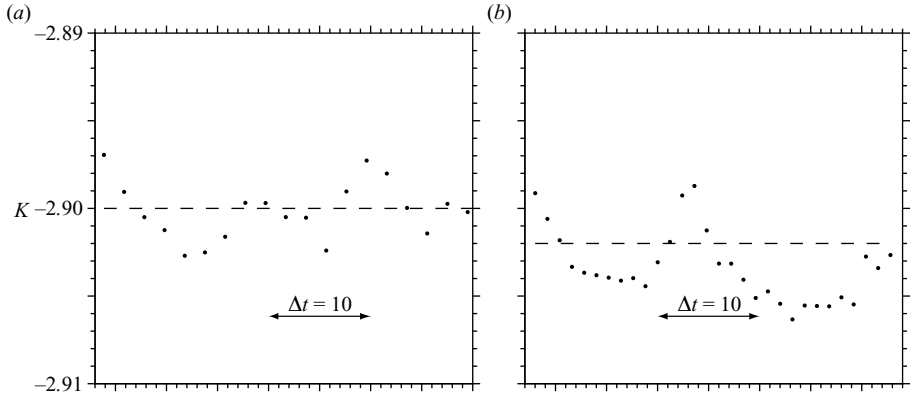

FIGURE 16. Kurtosis K of the core region PDF for (*a*) $Ra = 3.5 \times 10^6$ and (*b*) $Ra = 3.5 \times 10^7$ as a function of time t. The dashed lines (– –) indicate the ensemble average specified in table 2.

4.3. *Thermal dissipation rate contributions*

In order to analyse the contributions of different flow field features to the volume averaged thermal dissipation rate, the respective PDFs of regions *a–c* of each instantaneous flow field of a time series are integrated. Hence, the contribution from these regions can be quantified. Additionally the contributions due to the turbulent fluctuations are investigated by subtracting contributions due to the mean temperature gradient. The results are given in table 3 and compared to the contributions estimated through the integration of regions I to III provided by the same table.

It follows from table 3 (top) that the relative contribution from the subdomain representing the core region *a* increases with Rayleigh number until a fully developed turbulent temperature field is achieved. Integration over the bulk (region I) on the other hand shows that its contribution remains approximately constant in the range of *Ra* considered. This implies that heat dissipation is redistributed from the sidewalls to the core region. In their experiments Zhou & Xia (2002) found that the thermal plumes are predominately rising along the sidewalls. However, at sufficiently high *Ra* increasingly more plumes seem to be propagating through the interior cell which can also be seen from the instantaneous flow fields presented in figure 3. Shishkina & Wagner (2007*b*) have shown that the distribution of the local heat fluxes perpendicular

to the vertical walls becomes more uniformly distributed with increasing Ra, implying an increasing core contribution. Analysis of the fluctuating component of the thermal dissipation rates shows that contributions due to the mean temperature gradient are negligible in the core which is consistent with experimental results by He *et al.* (2007). On the other hand turbulent fluctuations of the bulk region increase and thus approach the behaviour of the core, since mean gradient contributions near the adiabatic walls decrease rapidly as Ra increases. This suggests that the effect of the adiabatic sidewalls on the flow is reduced as Ra increases.

It also follows from the table that contributions of plumes and boundary layers, i.e. the sum of the contributions of regions II and III, are approximately constant. Contrary to this contributions due to region b slightly decrease with Ra, whereas the intermediate layer contributions increase again for $Ra > 3.5 \times 10^7$. This is certainly the case because the condition for separating the plumes and boundary layers by a temperature threshold based on the mean temperature at the edge of the boundary layer is not sufficient, since effects of intermittency cannot be distinguished. However, table 3 (bottom) illustrates that the conductive sublayer contributions become less important as Ra increases. This indicates that the plumes despite their decreasing size are convecting increasingly more heat as Ra increases. On the other hand the contributions of the sublayer region due to turbulent fluctuations increase significantly from about 18 % to 73 % from the lowest to the highest Ra. Therefore it has to be pointed out, that with increasing Ra turbulent thermal fluctuations play an important role in the near-wall region. Despite the fact that the plumes and mixing layers contribute increasingly more to the heat transport, it is observed that their contributions due to turbulent fluctuations decrease which agrees with findings by He *et al.* (2007). Therefore, we summarize that increasing buoyancy forces acting on the plumes result in a more turbulent sublayer caused by the impact of the oncoming plumes, whereas the plumes are less disturbed by the surrounding turbulence.

5. Conclusions

Three DNS and two high-resolved LES have been performed in the range $3.5 \times 10^5 \leqslant Ra \leqslant 2.31 \times 10^8$. The *a posteriori* estimated Kolmogorov and Batchelor scales show that the resolution of the DNS is sufficiently high, whereas in the LES only the boundary layers are well resolved and the grid spacing in the core region is of the same order of magnitude as the Kolmogorov scales. Two major analyses are carried out, the first concentrating on the interaction between the temperature and the velocity fields and the second focusing on the evaluation of the thermal dissipation rates that are associated with different features of the flow.

The analysis of the PDFs of the thermal dissipation rates highlights that there exist three distinct regions that are dominated by the turbulent background or bulk I and the conductive sublayer III, which are separated by dissipation rates dominated by the plumes and mixing layers II. These regions are separated by the two inflection points of the thermal dissipation rate PDFs. It was shown that the core region a and the intermediate layer c together give a good representation of the bulk region I. Furthermore the tails of the PDFs of regions I and III correlate very well with the respective PDFs of the subdomains a (core region) and b (conductive sublayer).

The investigation of the core region reveals that the turbulent thermal dissipation rates have a complex three-dimensional distribution at low Rayleigh numbers and are more evenly distributed at the highest Ra. This suggests that turbulent mixing rather

than buoyancy begins to dominate this region. This argument is supported by the analysis of the turbulent fluctuations of the temperature and the velocity field. At high Ra, $|\boldsymbol{u}|'$ and θ' are only weakly correlated in the core and increasingly less turbulent thermal energy is contained in the core region as Ra increases. Therefore, the core region is hardly affected by buoyancy at high Ra, which is why the thermal dissipation rates are beginning to form a plateau as Ra increases, but show a more complex distribution at lower Ra, where the flow is not sufficiently mixed and buoyancy effects can be observed. A comparison of the PDFs of the thermal dissipation rates with a theoretically predicted scaling law by Chertkov *et al.* (1998) and Gamba & Kolokolov (1999) suggests that with increasing Ra the core region is slowly approaching the behaviour of a passively mixed scalar. However, the simulated Ra are not sufficiently high to prove this behaviour. By integration of the PDFs of the bulk (region I) and the core (region a), it is found that the dissipation of heat near the adiabatic walls is decreasing and is increasing in the core, which reflects an increasing propagation of the plumes through the centre. Evaluation of the fluctuating components of the thermal dissipation rates reveals that contributions due to the mean temperature gradient are negligible in the core which is in agreement with experimental findings by He *et al.* (2007). However, we find that in the range of Ra considered the contributions of the core region increase with Ra even though the thermal dissipation rates in the bulk decrease as stated by He *et al.* (2007).

The analysis of the thermal dissipation rates of the boundary layers including the plumes (sum of region II and III) reflects that their contribution is constant over the simulated range of Ra. On the contrary contribution from region b, i.e. the plumes and boundary layers separated through $|\theta| > |\theta_e|$ decreases slightly with Ra. This shows that effects of intermittency grow and parts of the boundary layer and plumes region are not detected through the temperature threshold criterion. Integration of the PDFs of region II reveals that with increasing Ra the plume-dominated region contributes increasingly more to the volume-averaged thermal dissipation rate. The thermal dissipation rate contributions of region III on the other hand are reduced by approximately the same amount, which seems logical given that convective heat transport becomes increasingly important at high Rayleigh numbers. This is also supported by the results obtained by calculating the contributions of the fluctuating components ϵ'_θ to region b showing that their contribution to the boundary layer's thermal dissipation rate is increasing from 37 % at $Ra = 3.5 \times 10^5$ to 42 % at $Ra = 3.5 \times 10^7$. Here, our results contradict findings by He *et al.* (2007) who experimentally measured a decrease of the fluctuations of the thermal dissipation rates in the near-wall region, whereas we find an increasing contribution of the fluctuations to the boundary layer dissipation rates. It was also shown that $\overline{\epsilon'_\theta}$ increases in the vicinity of the conducting walls. Hence, we conclude that He *et al.* (2007) measured the fluctuations in the boundary layer, but not within the conductive sublayer where we find the contrary to their findings. Therefore, we come to the conclusion that the conductive sublayer and the plumes/mixing layers behave dynamically different. A comparison of the kinetic and thermal dissipation rates has shown that their ratio is reduced from approximately 1.4 to unity from the lowest to the highest Ra. This highlights that there are increasingly stronger interactions between the temperature and the velocity fields which are underlined by a strong correlation of the velocity and the temperature fluctuations near the wall, whereas the opposite is found in the core region. The different dynamics of both fields are also reflected by the turbulent energy of the different scales, since the maximum turbulent thermal energy is located at the edge of the thermal boundary layers, whereas the turbulent kinetic energy

is further increasing towards mid-cell. Furthermore, no characteristic thermal scales could be observed at high Ra, but a large-scale wind was still maintained.

In order to further verify the assumption that region II represents the plume-dominated thermal dissipation rates it might be desirable to set different threshold values for each horizontal plane, to separate plumes and boundary layers more adequately as suggested by Shishkina & Wagner (2008).

Time series of the least-squarefit coefficients of the conductive sublayer PDFs was used to estimate a dimensionless global plume shedding frequency of 0.2–0.1. However, time series of the kurtosis of the boundary layer PDFs does not yield such strong fluctuations, but tends to show a much slower oscillation.

Finally, the increasing gradient of the thermal dissipation rate PDFs for $\zeta \approx 1$ implies that a distinct boundary between the thermal dissipation rates associated with the bulk flow and the plumes/boundary layer regions is formed. Hence, it is concluded that the assumption to split the thermal dissipation rates into contributions from plumes (including boundary layers) and the background as stated by (1.3) is indeed reasonable. However, we would like to point out that a relatively smooth transition of the probability of the thermal dissipation rates from regions I (bulk) to III (conductive sublayer) is observed for the lowest simulated Ra. At high Ra on the other hand the thermal plumes seem to play a crucial role, linking regions I and III. This is also reflected by their increasing contribution to the mean heat transport. Hence, we conclude that at high Ra the contributions of the thermal plumes to the mean heat transport must not be neglected, which supports the argument by the Grossmann–Lohse theory. However, our results have shown that $\hat{\epsilon}_{\theta,plume}$ might be separated into contributions due to the conductive sublayers and the plumes/mixing layers.

The authors would like to thank Olga Shishkina and Jörg Schumacher for fruitful discussions and their suggestions. This work was supported by the Helmholtz Association (HGF) through the project Virtual Institute – Thermal Convection.

REFERENCES

Belmonte, A., Tilgner, A. & Libchaber, A. 1994 Temperature and velocity boundary layers in turbulent convection. *Phys. Rev.* E **50** (1), 269–279.

Bolgiano, R. 1959 Turbulent spectra in a stably stratified atmosphere. *J. Geophys. Res.* **64** (12), 2226–2229.

Castaing, B., Gunarante, G., Heslot, F., Kadanoff, L., Liebchaber, A., Thomae, S., Wu, X., Zaleski, S. & Zanetti, G. 1989 Scaling of hard thermal turbulence in Rayleigh–Bénard convection. *J. Fluid Mech.* **204**, 1–30.

Chertkov, M., Falkovich, G. & Kolokolov, I. 1998 Intermittent dissipation of a passive scalar in turbulence. *Phys. Rev. Lett.* **80** (10), 2121–2124.

Gamba, A. & Kolokolov, I. V. 1999 Dissipation statistics of a passive scalar in a multidimensional smooth flow. *J. Stat. Phys.* **94**, 759–777.

Grossmann, S. & Lohse, D. 2000 Scaling in thermal convection: a unifying theory. *J. Fluid Mech.* **407**, 27–56.

Grossmann, S. & Lohse, D. 2004 Fluctuations in turbulent Rayleigh–Bénard convection: the role of plumes. *Phys. Fluids* **16** (12), 4462–4472.

Grötzbach, G. 1983 Spatial resolution requirements for direct numerical simulation of Rayleigh–Bénard convection. *J. Comp. Phys.* **49**, 241–264.

Hartlep, T. 2004 Strukturbildung und Turbulenz. Eine numerische Studie zur turbulenten Rayleigh-Bénard Konvektion. PhD thesis, Universität Göttingen.

Hartlep, T., Tilgner, A. & Busse, F. H. 2005 Transition to turbulent convection in a fluid layer heated from below at moderate aspect ratio. *J. Fluid Mech.* **554**, 309–322.

He, X., Tong, P. & Xia, K.-Q. 2007 Measured dissipation field in turbulent Rayleigh–Bénard convection. *Phys. Rev. Lett.* **98** (14).

Kraichnan, R. H. 1962 Turbulent thermal convection at arbitrary Prandtl number. *Phys. Fluids* **5**, 1374–1389.

Leonard, A. & Winkelmans, G. S. 1999 A tensor-diffusivity subgrid model for Large-Eddy Simulation. *Tech. Rep.* 043. Caltech ASCI.

Lohse, D. 1994 Temperature spectra in shear flow and thermal convection. *Phys. Lett.* A **196**, 70–75.

Maystrenko, A., Resagk, C. & Thess, A. 2007 Structure of the thermal boundary layer for turbulent Rayleigh–Bénard convection of air in a long rectangular enclosure. *Phys. Rev.* E **75** (6), 066303.

Niemela, J. J., Skrbek, L., Sreenivasan, K. R. & Donelly, R. J. 2000 Turbulent convection at very high Rayleigh numbers. *Nature* **404**, 837–840.

Oboukhov, A. M. 1962 Some specific features of atmospheric turbulence. *J. Fluid. Mech.* **13**, 77–81.

du Puits, R., Resagk, C., Tilgner, A., Busse, F. H. & Thess, A. 2007 Structure of thermal boundary layers in turbulent Rayleigh–Bénard convection. *J. Fluid Mech.* **572**, 231–254.

Roche, P. E., Castaing, B. & Hebral, B. 2001 Observation of the 1/2 power law in Rayleigh–Bénard convection. *Phys. Rev.* E **63**.

Schumacher, J. & Sreenivasan, K. R. 2005 Statistics and geometry of passive scalars. *Phys. Fluids* **17** 125107.

Schumann, U., Grötzbach, G. & Kleiser, L. 1979 Direct numerical simulations of turbulence. In *Prediction Methods for Turbulent Flows*, VKI-lecture series 1979 2. Von Kármán Institute for Fluid Dynamics.

Shishkina, O. & Wagner, C. 2006 Analysis of thermal dissipation rates in turbulent Rayleigh–Bénard convection. *J. Fluid Mech.* **546**, 51–60.

Shishkina, O. & Wagner, C. 2007*a* Boundary and interior layers in turbulent thermal convection in cylindrical containers. *Int. J. Sci. Comp. Math.* **1** (2/3/4), 360–373.

Shishkina, O. & Wagner, C. 2007*b* Local heat fluxes in turbulent Rayleigh–Bénard convection. *Phys. Fluids* **19** (8), 085107–1–085107–13.

Shishkina, O. & Wagner, C. 2008 Analysis of sheetlike thermal plumes in turbulent Rayleigh–Bénard convection. *J. Fluid Mech.* **599**, 383–404.

Shraiman, B. I. & Siggia, E. D. 1990 Heat transport in high-Rayleigh-number convection. *Phys. Rev.* A **42**, 3650–3653.

Swarztrauber, P. N. 1974 A direct method for the discrete solution of separable elliptic equations. *SIAM J. Num. Anal.* **11**, 1136–1150.

Verzicco, R. & Camussi, R. 2003*a* Numerical experiments on strongly turbulent thermal convection in a slender cylindrical cell. *J. Fluid Mech.* **477**, 19–49.

Verzicco, R. & Camussi, R. 2003*b* Turbulent thermal convection in a closed domain: viscous boundary layer and mean flow effects. *Eur. Phys. J. B.* **35**.

Verzicco, R. & Sreenivasan, K. R. 2008 A comparison of turbulent thermal convection between conditions of constant temperature and constant heat flux. *J. Fluid Mech.* **595**, 203–219.

Xi, H.-D., Lam, S. & Xia, K.-Q. 2004 From laminar plumes to organized flows: the onset of large-scale circulation in turbulent thermal convection. *J. Fluid Mech.* **503**, 47–56.

Zhou, S.-Q. & Xia, K.-Q. 2002 Plumes statistics in thermal turbulence: mixing of an active scalar. *Phys. Rev. Lett.* **89** (18), 184502.